**Wim-Paul Breugem**
Laboratory for Aero and Hydrodynamics,
Delft University of Technology,
Leeghwaterstraat 21,
Delft CA 2628, The Netherlands
e-mail: w.p.breugem@tudelft.nl

**Vincent van Dijk**
IHC Merwede,
Smitweg 6,
Kinderdijk AW 2961, The Netherlands
e-mail: v.vandijk@mtiholland.com

**René Delfos**
Laboratory for Aero and Hydrodynamics,
Delft University of Technology,
Leeghwaterstraat 21,
Delft CA 2628, The Netherlands
e-mail: r.delfos@tudelft.nl

# Flows Through Real Porous Media: X-Ray Computed Tomography, Experiments, and Numerical Simulations

*Two different direct-forcing immersed boundary methods (IBMs) were applied for the purpose of simulating slow flow through a real porous medium: the volume penalization IBM and the stress IBM. The porous medium was a random close packing of about 9000 glass beads in a round tube. The packing geometry was determined from an X-ray computed tomography (CT) scan in terms of the distribution of the truncated solid volume fraction (either 0 or 1) on a three-dimensional Cartesian grid. The scan resolution corresponded to 19.3 grid cells over the mean bead diameter. A facility was built to experimentally determine the permeability of the packing. Numerical simulations were performed for the same packing based on the CT scan data. For both IBMs the numerically determined permeability based on the Richardson extrapolation was just 10% lower than the experimentally found value. As expected, at finite grid resolution the stress IBM appeared to be the most accurate IBM.* [DOI: 10.1115/1.4025311]

## 1 Introduction

Porous media are characterized by an open solid structure with interconnected pores through which a fluid may flow. Examples of porous media are pebble bed nuclear reactors, packed beds in the chemical industry, river beds composed of granular material, and gas/oil reservoirs of porous rock such as sandstone. Until recently, it was neither possible to measure nor to simulate the flow within the pores of such beds because of their complex geometry. It is partly for this reason that in the past many studies were devoted to flows in *idealized* porous media composed of cylinders, spheres, or cubes in a typically ordered (spatially periodic) configuration [1–3]. With the ever-increasing computer power, the development of efficient numerical methods, and imaging methods such as X-ray computed tomography (CT), it has now become possible to study flows in *real* porous media with the help of numerical simulations.

Narsilio et al. [4] used high-resolution X-ray CT to obtain three-dimensional images of a packing of glass beads. They simulated the flow through the reconstructed pore geometry with a commercial finite-element package and validated their numerical results for the hydraulic conductivity with experiments. A similar study was performed by Kaczmarczyk et al. [5,6] to numerically determine the permeability of carbonate rock samples and by Zeretskiy et al. [7] to study flow and solute transport through sandstone. Ovaysi and Piri [8] used a moving particle semi-implicit (mesh-free) method to simulate flow through sandstone. Gerbaux et al. [9] used both a finite-volume and a lattice-Boltzmann method for studying flows through metallic foams.

In this paper, we explore the use of a finite-volume method combined with a computationally efficient immersed boundary method (IBM) [10] for simulating flows through real porous media. The essence of IBMs is that the flow geometry is immersed in a three-dimensional computational grid. Instead of imposing the no-slip/no-penetration conditions at fluid-solid interfaces, forces are imposed on the fluid in order to enforce these conditions by good approximation. The main advantage of IBMs is the possibility of using simple (often regular) grids, which enables the use of simple discretization stencils and computationally efficient solvers. *Continuous-forcing* IBMs were recently employed by Smolarkiewicz and Winter [11] to study flow through numerically generated random porous media and by Lopez Penha et al. [12] for flow through an array of square rods. For the present study, we employed two different *direct-forcing* IBMs for studying flow through a packing of glass beads: the volume penalization IBM of Kajishima et al. [13] and the stress IBM of Breugem and Boersma [3] and Pourquie et al. [14]. The geometry of the packing was obtained from an X-ray CT scan. In order to validate the simulations, a facility was built to experimentally determine the permeability of the packing.

Pore-scale simulations of real porous media provide a detailed insight in the flow dynamics. From such simulations the permeability $K$ of a porous medium can be numerically determined. The permeability is a measure of the ability of a porous medium to transmit fluid through its pores. Once the permeability is known, the pressure drop over a porous medium can be computed from Darcy's law [15]

$$0 = -\frac{\partial \langle p \rangle}{\partial z} - \frac{\mu \langle w \rangle^s}{K} \tag{1}$$

where $\langle p \rangle$ is the so-called intrinsic macroscopic pressure, $\langle w \rangle^s$ is the superficial macroscopic velocity, and $\mu$ is the dynamic viscosity of the fluid. The brackets denote that the quantities are locally averaged over a small spatial volume [16]: here, $\langle w \rangle^s \equiv \int_V m\gamma w dV$, where $m$ is a weighting function and $\gamma$ is the phase-indicator function (equal to 1 in the fluid phase and 0 in the solid phase). The size of the averaging volume $V$ has to be sufficiently large to average out pore-scale inhomogeneities in the flow field, but should be small enough to maintain variations in the flow field on a macroscopic scale [3]. When the superficial volume average is divided by the porosity $\varepsilon \equiv \int_V m\gamma dV$, the intrinsic volume average is obtained.

For packed beds many different semi-empirical relations exist in which the permeability is expressed as a function of the so-called mean particle diameter $d_p$ and the porosity $\varepsilon$. (The mean

Contributed by the Fluids Engineering Division of ASME for publication in the Journal of Fluids Engineering. Manuscript received March 6, 2013; final manuscript received August 27, 2013; published online February 28, 2014. Assoc. Editor: Elias Balaras.

  

particle diameter is defined as six times the volume of the particles of the packing divided by their total surface area; for perfectly monodisperse spheres it is exactly equal to the sphere diameter.) One of the most often used expressions for the permeability is given by the (modified) Ergun equation [17,18]

$$K = \frac{d_p^2 \varepsilon^3}{C_{\mathrm{ME}}(1-\varepsilon)^2} \tag{2}$$

where $C_{\mathrm{ME}}$ is a constant. MacDonald et al. [18] proposed a value of $C_{\mathrm{ME}} = 180$, although the experimental scatter in $C_{\mathrm{ME}}$ is large. In this study we consider a packing of glass beads. Experimental data from Gupte [19] actually suggest that a value of $C_{\mathrm{ME}} \approx 160$ is more appropriate for such a packing.

Darcy's law is valid for sufficiently slow flow through a porous medium such that the flow within the pores is in the Stokes regime. For packed beds this appears to hold when the packed bed Reynolds number is smaller than $O(10)$ [17]. This Reynolds number is defined as $\mathrm{Re}_p \equiv \rho d_p \langle w \rangle^s / (\mu[1-\varepsilon])$, where $\rho$ is the fluid mass density. The values of $\mathrm{Re}_p$ in the experiments and simulations in this study are of $O(1)$ and thus in the regime where Darcy's law is expected to be valid.

The structure of this paper is as follows: First the experiments are detailed. Next, the procedure used to obtain the geometry of the packing of glass beads from an X-ray CT scan is described. Then, the details of the computational method and the two IBMs used are given. Subsequently, results from the numerical simulations are shown. Finally, the last section contains the main conclusions.

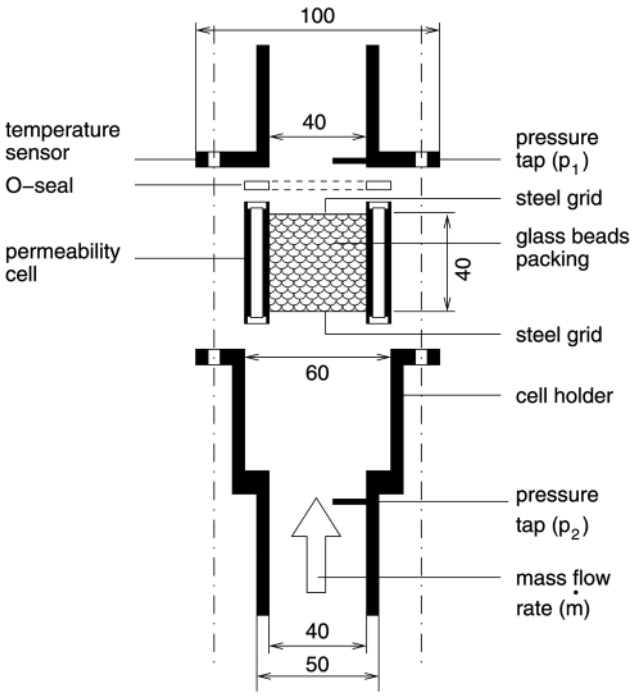


**Fig. 1 Close-up of the experimental setup showing the permeability cell, the cell holder, and the locations of the pressure taps and temperature sensor. Dimensions are given in mm.**

## 2 Experimental Setup and Measurement Results

**2.1 Experimental Setup.** A facility has been built to experimentally determine the permeability of the packing of glass beads. It was designed such that the packing could be easily removed from the setup to place it into a CT scanner. The packing was tightly fixed in a cylindrical permeability cell of PVC by two fairly coarse but thin-wired steel grids. Because they are spanned over the glass beads, their shape is slightly convex (as is visible in Fig. 5(*a*)). The permeability cell was placed in a holder, as sketched in Fig. 1. An O-seal was placed in between the permeability cell and the top part of the holder to prevent by-pass leakage. The top and bottom part of the holder were mounted together by six plastic plugs.

The glass beads are nearly spherical with a fairly narrow size distribution; the beads were sieved between a diameter of 1.66 and 2 mm. A pycnometer and a lab balance were used to determine the volume taken up by the glass beads and their total mass. The total volume taken up by the packing, including the volume of the pores, was estimated from the average streamwise length of the packing $L_c = 42 \pm 1$ mm and the inner radius of the cylindrical permeability cell $R_c = 20.1 \pm 0.1$ mm. Next, the *global* porosity[1] of the packing could be estimated as $\varepsilon = 0.367 \pm 0.009$ [20]. The packing can thus be classified as a *random close packing* [21]. The mass of a few samples of each 100 glass beads was measured with a lab balance. From this and the measured total mass of the glass beads, the total number of glass beads could be estimated as $N_p = 8.92 \pm 0.16 \times 10^3$. Finally, from the total volume and the total number of particles, the mean particle diameter was determined to be $d_p = 1.93 \pm 0.01$ mm.

The experiments were designed such that the packed bed Reynolds number in the experiments is $O(1)$, i.e., within the range where Darcy's law is valid. Furthermore, the size of the permeability cell had to be small enough to fit inside the CT scanner. The resolution restrictions of the CT scanner and the numerical simulations required that the particles were not too small compared to the size of the permeability cell.

The experimental setup is a closed system in which the flow direction through the permeability cell is opposite to the direction of gravity (i.e., upward) for the sake of easy removal of air bubbles and in order to reduce the deposition of dirt within the cell. The working fluid is an aqueous solution of glycerol with about 70% by weight of glycerin. The dynamic viscosity was measured within 1% accuracy with a Contraves low shear 40 viscometer at $T = 20 \pm 0.1\,^{\circ}\mathrm{C}$, from which the real percentage of glycerin could be inferred. The temperature of the fluid is measured downstream of the permeability cell with a PT100 temperature sensor with 0.1 °C accuracy. Then the dynamic viscosity at that temperature is determined from an empirical formula proposed by Cheng [22]. The flow is driven by a constant-flow gear pump that is controlled by a variable-frequency drive. The mass flow rate is measured by collecting the outflow in a measuring cup placed on a lab balance and measuring the discharge time with a stopwatch. The pressure drop over the permeability cell is measured with a differential pressure transducer (Validyne DP15 with Dash-28 membrane; range $5.5 \times 10^3$ Pa). The pressure tubes are connected through bleed screws with the pressure chambers of the transducer and, hence, the hydrostatic contribution disappears from this differential pressure measurement. The transducer was calibrated with a Betz water column manometer with an accuracy of of 1 Pa. A simple USB data acquisition device (National Instruments USB-6009) and a LabVIEW program are used to read the electronic output of the instruments, after which the data is further processed.

**2.2 Measurement Results.** The experiments were performed at five different pump frequencies in one day and repeated the next day. At every pump frequency several measurements were performed in order to estimate the experimental uncertainty. To determine the permeability of the packing from the experiments, Darcy's law [1] is rewritten in the following form

[1]The global should be distinguished from the *local* porosity, which could be calculated from $\varepsilon \equiv \int_V m\gamma dV$ with an appropriate choice of the weighting function $m$. The local porosity is expected to vary with the radial distance to the wall of the permeability cell. This causes radial variations in the flow near the wall and is known as the wall-channeling effect [19].

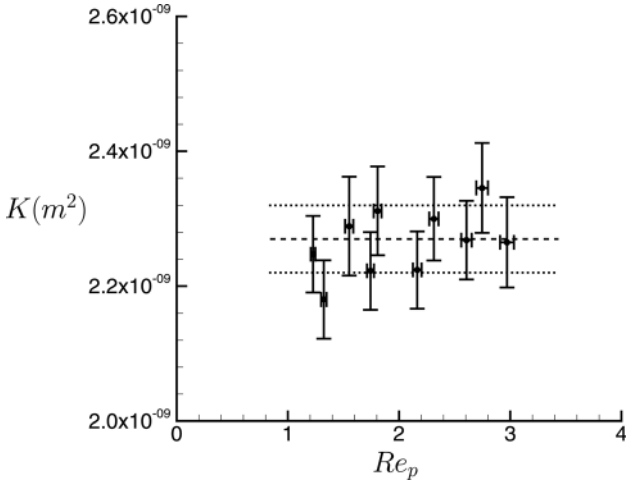


**Fig. 2 Measured permeability as a function of the packed bed Reynolds number. The horizontal and vertical error bars denote the estimated standard deviation in both quantities. The dashed line is the average value for the permeability. The dotted lines show the standard deviation in the average value based on the spreading in the data points.**

$$K = \mu\left(\frac{L_c}{p_2 - p_1}\right)\left(\frac{\dot{m}}{\rho\pi R_c^2}\right) \tag{3}$$

where $p_2 - p_1$ is the measured pressure difference over the permeability cell and $\dot{m}$ is the measured mass flow rate. Figure 2 depicts the permeability as a function of the packed bed Reynolds number. The average permeability and its 95% confidence interval are determined to be $K = 2.27 \pm 0.03 \times 10^{-9}$ m$^2$. This value is in fairly good agreement with the predicted value of $K = 2.55 \times 10^{-9}$ m$^2$ from the modified Ergun equation (2) with $C_{\mathrm{ME}} = 180$, especially when considering the uncertainty in the value of $C_{\mathrm{ME}}$. Compared to the predicted value, the measured value is about 11% smaller. It would match the prediction when $C_{\mathrm{ME}} \approx 215$ would be taken. Compared to the value of $C_{\mathrm{ME}} \approx 160$ suggested from the data of Gupte [19], our estimate of $C_{\mathrm{ME}}$ is roughly 30% higher; it is difficult to assess the origin of this difference since Gupte's Ph.D. thesis, with the details of his experiments, is not easily accessible.

It is noted that the permeability is quite sensitive to the values of the porosity and the mean particle diameter. As previously mentioned, for $C_{\mathrm{ME}} = 180$, $d_p = 1.93$ mm, and $\varepsilon = 0.367$, the modified Ergun equation (2) predicts a permeability of $K = 2.55 \times 10^{-9}$ m$^2$. A variation of the porosity by $\pm 3\%$ with the values of $C_{\mathrm{ME}}$ and $d_p$ fixed, would result in a variation in the permeability from $-12\%$ to $+13\%$. Similarly, a variation of $d_p$ by $\pm 3\%$ would yield a variation in the permeability from $-6\%$ to $+6\%$. This emphasizes the importance for an accurate determination of the porosity and the mean particle diameter in order to accurately determine the value of $C_{\mathrm{ME}}$.

## 3 X-Ray Computed Tomography

The geometry of the packing of glass beads has been obtained from a high-resolution X-ray computed tomography (CT) scanner at the Delft University of Technology (Phoenix Nanotom s from GE). Prior to the experiments, the permeability cell with the packing of glass beads was placed on an object table inside the scanner, located in between the X-ray tube and the detector. The permeability cell was dry, i.e., the pores of the packing were air-filled. The object table was rotated over small angular steps and shifted in the vertical direction in order to measure the attenuation of the X-ray by the permeability cell for a large number of lines.

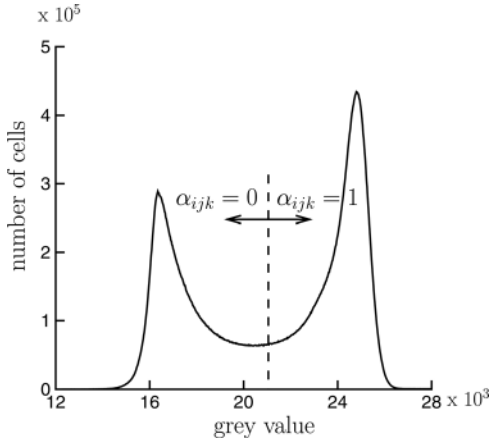


**Fig. 3 Histogram of the cell gray values as computed from the X-ray CT scan with a bin size of 24 in the gray value. The dashed line marks the threshold gray value used for determining the value of the cell solid volume fraction ($\alpha_{ijk} = 0$ for air and 1 for glass).**

From this a three-dimensional image of the permeability cell was reconstructed.

The output data of the scanner is a three-dimensional Cartesian grid of cells with 'gray values' representing the attenuation of the X-ray in every cell. The scan used in the present study contains $412 \times 412 \times 486$ grid cells in the two spanwise and the streamwise directions, respectively, with the dimension of the cubical cells equal to 0.1 mm. As shown in Fig. 3, the distribution of gray values contains two clear peaks associated with the air in the pores and the glass beads, respectively. A threshold gray value was chosen in between the two peaks. All cells with a gray value above this threshold value were associated with glass beads and $\alpha_{ijk} = 1$, while cells with a gray value below this threshold were associated with pores and $\alpha_{ijk} = 0$. This resulted in a *staircase* representation of the packing of the glass beads. In addition, in all grid cells at a radial distance from the centerline greater than the tube radius $R_c$, $\alpha_{ijk} = 1$ was imposed. Next, the porosity of the packing was numerically determined based on the distribution of $\alpha$. By varying the threshold value the numerical value for the porosity was matched with the experimentally determined value of the porosity ($\varepsilon = 0.367$). The threshold value was established at 21,050, which is indicated by the dashed line in Fig. 3. Cross sections of the solid volume fraction distribution are shown in Figs. 5 and 6.

The porosity varies nearly linearly as a function of the threshold gray value near the currently chosen value of 21,050 (not shown). When the threshold gray value is varied from 20,650 to 21,450, the porosity increases from 0.348 to 0.387, corresponding to a change of approximately 11.5%. This emphasizes the importance of carefully determining the threshold gray value, since the permeability is sensitive to the value of the porosity (see the discussion at the end of Sec. 2.2).

As an alternative to the present approach in which we truncate $\alpha$, one could also choose to smoothly vary $\alpha$ between 0 and 1 by using a narrow S-shaped function centered around a threshold gray value. The width of the S-shaped function can be chosen such that it matches the X-ray CT scan resolution. The threshold gray value can be adapted in a similar vein, as previously described, in order to match the numerical value of the porosity with the experimentally determined value. This option is left for future research.

## 4 Computational Method

**4.1 Governing Equations.** The governing equations for the flow field in the pores of the porous medium are the incompressible Navier–Stokes equations, which read

$$\nabla \cdot \mathbf{u} = 0 \tag{4a}$$

$$\frac{\partial \mathbf{u}}{\partial t} + \nabla \cdot \mathbf{uu} = -\frac{1}{\rho}\nabla p + \nu \nabla^2 \mathbf{u} \tag{4b}$$

where $\mathbf{u}$ is the velocity, $p$ is the modified pressure (i.e., the actual pressure minus the contribution from the hydrostatic pressure), and $\nu \equiv \mu/\rho$ is the kinematic viscosity. For flows through rigid porous media these equations have to be solved with the no-slip/no-penetration (ns/np) conditions for the velocity at the fluid-solid interfaces.

**4.2 Numerical Scheme and Flow Geometry.** As mentioned in the Introduction section, in an IBM the ns/np conditions are not directly imposed, but a force $\mathbf{f}$ is added to the right-hand side of Eq. (4*b*) in order to enforce these conditions by a good approximation. The IBMs considered in this study are the volume penalization IBM of Kajishima et al. [13] and the stress IBM of Breugem and Boersma [3] and Pourquie et al. [14]. Both IBMs fall in the class of direct (or *discrete*) forcing methods, since the additional forcing from the IBM is not parameterized prior to discretization as in continuous forcing methods, but directly embedded in the discretization scheme used [10]. The two IBMs differ from each other in the way in which the force $\mathbf{f}$ is computed, as detailed in the next section.

The direct-forcing IBMs used for this study are embedded in a standard finite-volume/pressure-correction scheme. The integration in time is based on the Crank–Nicolson scheme for the pressure-gradient term and the Adams–Bashforth scheme for all other terms; both schemes are second-order accurate in time. In semidiscrete notation, the scheme reads as follows

$$\mathbf{u}^* = \mathbf{u}^n + \frac{\Delta t}{\rho}\left(-\nabla p^{n-1/2} + \frac{3}{2}\mathbf{rhs}^n - \frac{1}{2}\mathbf{rhs}^{n-1}\right) \tag{5a}$$

$$\mathbf{u}^{**} = \mathbf{u}^* + \Delta t \mathbf{f}^{n+1/2} \tag{5b}$$

$$\nabla^2 \tilde{p} = \frac{\rho}{\Delta t}\nabla \cdot \mathbf{u}^{**} \tag{5c}$$

$$\mathbf{u}^{n+1} = \mathbf{u}^{**} - \frac{\Delta t}{\rho}\nabla \tilde{p} \tag{5d}$$

$$p^{n+1/2} = p^{n-1/2} + \tilde{p} \tag{5e}$$

where $\mathbf{rhs} \equiv -\rho \nabla \cdot \mathbf{uu} + \mu \nabla^2 \mathbf{u}$, $\mathbf{u}^*$ is the first prediction velocity, $\mathbf{u}^{**}$ is the second prediction velocity that includes the additional forcing from the IBM, $\tilde{p}$ is the correction pressure, and $\Delta t$ is the computational time step.

The computational grid used in the simulations is a spatially uniform fully staggered Cartesian grid [23]. Spatial gradients are computed with the second-order central-differencing scheme. The spatially continuous grid, without any holes in the interior of the flow domain, enables the use of an efficient, FFT-based direct solver to compute the correction pressure from Eq. (5*c*). The computational time step is based on the von Neumann stability conditions for the second-order Adams–Bashforth scheme derived by Wesseling [24] (see p. 188). It is set to 0.75 times the maximum allowed value to ensure stability. For the creeping flow simulations in the present study and cubical grid cells $\Delta t = 0.75\Delta x^2/(12\nu)$.

The computational domain is a square channel with the geometry of the permeability cell centered in the middle; see Figs. 5(*a*) and 6(*a*). The dimensions of the channel are $41.4 \times 41.4 \times 48.6$ mm in the $x$-, $y$-, and $z$-directions, respectively. The spanwise dimensions of the channel were chosen slightly larger (0.2 mm) than the spanwise dimensions of the X-ray CT scan to ensure that the permeability cell fits well within the channel. In the simulations of the 'standard case,' the grid resolution is exactly the same as the CT scan resolution, i.e., $\Delta x = \Delta y = \Delta z = 0.1$ mm. The boundary conditions at the solid side walls of the square channel are the ns/np conditions for the velocities and the homogeneous Neumann condition for the pressure. The boundary conditions at the inlet of the channel are the free-slip conditions for the boundary-parallel velocity components ($u$ and $v$), a uniform streamwise velocity ($w = \langle w \rangle^s$) over the circular inlet of the permeability cell, a zero streamwise velocity outside the circular inlet, and the homogeneous Neumann condition for the pressure. The boundary conditions at the outlet of the channel are the free-slip conditions for the boundary-parallel velocity components and zero pressure. The streamwise velocity at the outlet of the channel is determined from the continuity equation (4*a*).

The discretized Navier–Stokes equations are made dimensionless with a reference velocity of 1 mm/s and a reference length of 1 mm. The kinematic viscosity is set equal to 12.8 mm$^2$/s, based on a typical value for the viscosity in the experiments. The superficial bulk velocity at the inlet of the permeability cell is determined from the requirement that the packed bed Reynolds number is equal to 1 in order to guarantee the validity of Darcy's law. From the definition of $\mathrm{Re}_p$ it then follows that $\langle w \rangle^s = \mathrm{Re}_p \nu (1-\varepsilon)/d_p = 4.20$ mm/s by assuming that $\varepsilon = 0.367$ and $d_p = 1.93$ mm (see Sec. 2.1).

The simulations are initiated by prescribing a streamwise velocity $w = \langle w \rangle^s$ at all grid cells within the cylindrical permeability cell (i.e., for $r < R_c$ with $r$ being the radial distance from the centerline of the channel). This includes the grid cells located inside the glass beads. After initialization the flow inside the glass beads is quickly decelerated and comes to rest by the forcing from the IBM. From Darcy's law (Eq. (1)), a typical time scale can be estimated for the flow in the pores to reach a steady state $t_D = K/\nu$. From the semi-empirical Ergun relation (2) with $C_{\mathrm{ME}} = 180$, the following *a priori* estimate for the permeability of the packing of glass beads can be given as $K = 2.55 \times 10^{-3}$ mm$^2$. On this basis, the flow time scale is estimated to be $t_D = 2 \times 10^{-4}$ s. This is on the order of the computational time step in the simulations $\Delta t = 0.4875 \times 10^{-4}$ s, thus a quick convergence of the simulations can be expected within a few tens of time steps. This is, indeed, confirmed by the simulations.

The computational algorithm detailed in this section is coded in Fortran with the MPI extension for parallel execution on multiprocessor machines with distributed memory. For the parallelization of the Navier–Stokes equations a standard domain decomposition method is used.

**4.3 Immersed Boundary Methods**

*4.3.1 Volume Penalization IBM.* In the volume penalization IBM of Kajishima et al. [13], the IBM force is computed as follows

$$\mathbf{f}_{ijk}^{n+1/2} = \alpha_{ijk}\frac{(\mathbf{u}_{\mathrm{fs}} - \mathbf{u}^*)_{ijk}}{\Delta t} \tag{6}$$

where $\alpha_{ijk}$ is the solid volume fraction in the grid cell with index $(i,j,k)$ and $\mathbf{u}_{\mathrm{fs}}$ is the velocity at the fluid-solid interface within this grid cell. In rigid porous media the interface is not moving and hence $\mathbf{u}_{\mathrm{fs}} = \mathbf{0}$. Substituting Eq. (6) into Eq. (5*b*) then yields the following equation for the second prediction velocity

$$\mathbf{u}_{ijk}^{**} = (1 - \alpha_{ijk})\mathbf{u}_{ijk}^{*} \tag{7}$$

If a grid cell is located fully inside the fluid phase where $\alpha_{ijk} = 0$, then $\mathbf{u}_{ijk}^{**} = \mathbf{u}_{ijk}^{*}$ and, thus, the first prediction velocity is left unchanged. On the contrary, inside the solid phase $\alpha_{ijk} = 1$ and $\mathbf{u}_{ijk}^{**} = \mathbf{0}$.

As mentioned in Sec. 4.2, in the present study the computational grid is fully staggered. This means that the solid volume fraction is defined at the cell centers, while the velocities are defined at the cell faces. Since the IBM force needs to be computed at the cell faces where the velocities are defined, linear

interpolation is used to interpolate the solid volume fraction from the two nearest cell centers towards a cell face. At the cell centers the solid volume fraction is either 0 or 1 (see Sec. 3), thus, at the cell faces the interpolated solid volume fraction is either 0, 0.5, or 1. This implies that the fluid-solid interfaces are actually smoothed over a distance of one grid cell.

Note that the IBM forcing is applied to the second prediction rather than the actual velocity itself; see Eq. (5*b*). The difference between the two velocities follows from Eq. (5*d*) and is equal to $-\Delta t \nabla \tilde{p}/\rho$. This difference is kept small by updating the pressure at every time step by the correction pressure; see Eq. (5*e*). For creeping flows in porous media, fluid inertia can be neglected and the flow can be considered as stationary. In this case, the correction pressure will eventually approach zero in the simulations, eliminating the error associated with the difference between the second prediction and the actual velocity. Furthermore, near the fluid-solid interfaces the normal component of Eq. (5*a*) then reduces to $0 = [-\nabla p + \mu \nabla^2 \mathbf{u}] \cdot \mathbf{n}$, with $\mathbf{n}$ being the unit normal to the interface. This is the correct behavior of the flow field near the fluid-solid interfaces. Note that this holds only when we split the pressure according to Eq. (5*e*); if $p^{n+1/2}$ would be used to correct the second prediction velocity, then $[\nabla p] \cdot \mathbf{n} = 0$ would hold at the fluid-solid interfaces, which would be inconsistent with the Navier–Stokes equations.

The volume penalization IBM is computationally efficient since it consists simply of one additional multiplication of the first prediction velocity by a 'penalization' factor $(1 - \alpha_{ijk})$, representing the fluid volume fraction in a grid cell with index $(i, j, k)$.

Apart from its efficiency, another advantage of this IBM is that the penalization is based on the local fluid volume fraction, which, for real porous media, can be obtained from several methods such as magnetic resonance imaging and X-ray computed tomography (see Sec. 3). It is, therefore, a suitable method for detailed simulations of real porous-media flows.

In the literature, other methods can be found which are similar to the volume penalization IBM of Kajishima et al. [13]. For instance, essentially the same approach was used later by Scotti [25] to simulate turbulent open-channel flow over a wall roughened with ellipsoidal grains. Finally, it is noted that this IBM is different from the penalized direct forcing method of Belliard and Fournier [26], which is actually better referred to as a penalized continuous forcing method, according to the classification of Mittal and Iaccarino [10].

*4.3.2 Stress IBM.* As explained in Sec. 3, the truncation of the solid volume fraction to either 0 or 1 resulted in a staircase representation of the packing of glass beads. The stress IBM of Breugem and Boersma [3] and Pourquie et al. [14] has been specifically developed for rectangular-shaped obstacles and can, therefore, be applied to this geometry.

In the stress IBM the solid geometry is immersed in a fully staggered rectangular grid such that the fluid-solid interfaces coincide exactly with the faces of the grid cells. As a result, the velocity nodes *on* the fluid-solid interfaces correspond to velocities directed *normal* to the interfaces. The velocity nodes which are half a grid cell spacing *away* from the interfaces correspond to velocities directed *parallel* to the interfaces. This is illustrated in Fig. 4. The dots, open circles, and crosses indicate the locations at which in the stress IBM additional forcing is applied to the flow.

At the velocity nodes on the fluid-solid interfaces and *inside* the solid phase (i.e., the dots and open circles in Fig. 4) the second prediction velocity is put to $\mathbf{u}^{**} = \mathbf{u}_{\mathrm{fs}} = \mathbf{0}$. This corresponds to a force $\mathbf{f}_n$ directed normal to the interface and is given by

$$\mathbf{f}_{n,ijk}^{n+1/2} = -\frac{\mathbf{u}_{ijk}^{*}}{\Delta t} \tag{8}$$

With the help of Eqs. (5*b*), (5*d*), and (5*e*) and a Taylor expansion, it then follows for the velocities on the fluid-solid interfaces

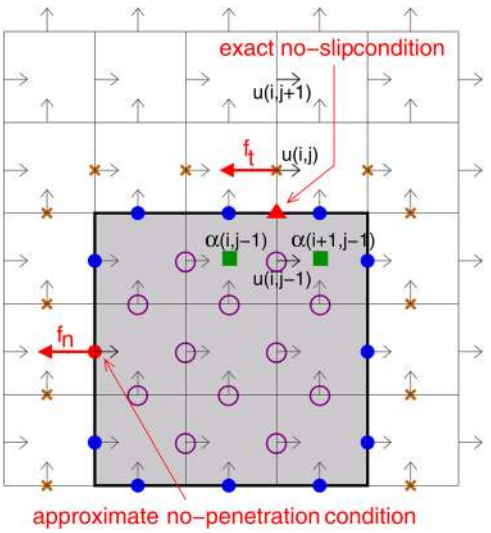


**Fig. 4 Illustration of the stress IBM of Breugem and Boersma [3] and Pourquie et al. [14] for rectangular-shaped obstacles. The crosses, dots, and open circles indicate the locations where additional forcing is imposed on the flow.**

$$\mathbf{u}_{ijk}^{n+1} = O\left(-\frac{\Delta t^2}{\rho} \cdot \left.\frac{\partial \nabla p}{\partial t}\right|^{n+1/2}\right) \tag{9}$$

From this it follows that for stationary flows $\mathbf{u}_{ijk}^{n+1} = \mathbf{0}$ holds (as desired), while for instationary flows $\mathbf{u}_{ijk}^{n+1} = O(\Delta t^2)$ holds and thus the error in the no-penetration condition can still be neglected provided that the time step is sufficiently small.

At the velocity nodes which are half a grid cell spacing away from the fluid-solid interfaces and located inside the fluid phase (i.e., the crosses in Fig. 4), the discretization stencils for the interface-normal advection and diffusion terms are adjusted such that the no-slip condition at the interfaces is satisfied exactly. As a 2D example, in the *absence* of a solid boundary the vertical diffusion term of streamwise momentum at node $(i,j)$ in Fig. 4 would read

$$\nu \left.\frac{\partial^2 u}{\partial y^2}\right|_{(i,j)} = \nu \left[\frac{u(i,j+1) - 2u(i,j) + u(i,j-1)}{\Delta y^2}\right] \tag{10a}$$

In the *presence* of a solid boundary, however, the desired discretization that accounts for the no-slip condition would read

$$\nu \left.\frac{\partial^2 u}{\partial y^2}\right|_{(i,j)} = \frac{\nu}{\Delta y}\left[\frac{u(i,j+1) - u(i,j)}{\Delta y} - \frac{u(i,j) - 0}{\Delta y/2}\right] \tag{10b}$$

The corresponding force $f_t$ at velocity node $(i,j)$ required for enforcing the no-slip condition at the solid-fluid interface thus becomes

$$f_t|_{(i,j)} = -\nu \left[\frac{u(i,j) - u(i,j-1)}{\Delta y^2}\right] \tag{10c}$$

The locations of the crosses where this force is applied is determined from the spatial distribution of the solid volume fraction in the surrounding grid cells. For example, the force $f_t$ at velocity node $(i, j)$ in Fig. 4 is applied when the sum $\alpha(i, j-1) + \alpha(i+1, j-1) \geq 1$.

The stress IBM thus prescribes the correct shear stress on a fluid-solid interface (hence, its name) and puts the velocity on the interface and within the solid phase to zero. It is a computationally efficient method with negligible overhead for computing the IBM forcing. As discussed by Pourquie et al. [14], the stress IBM usually has no or a negligible effect on the stability of the overall

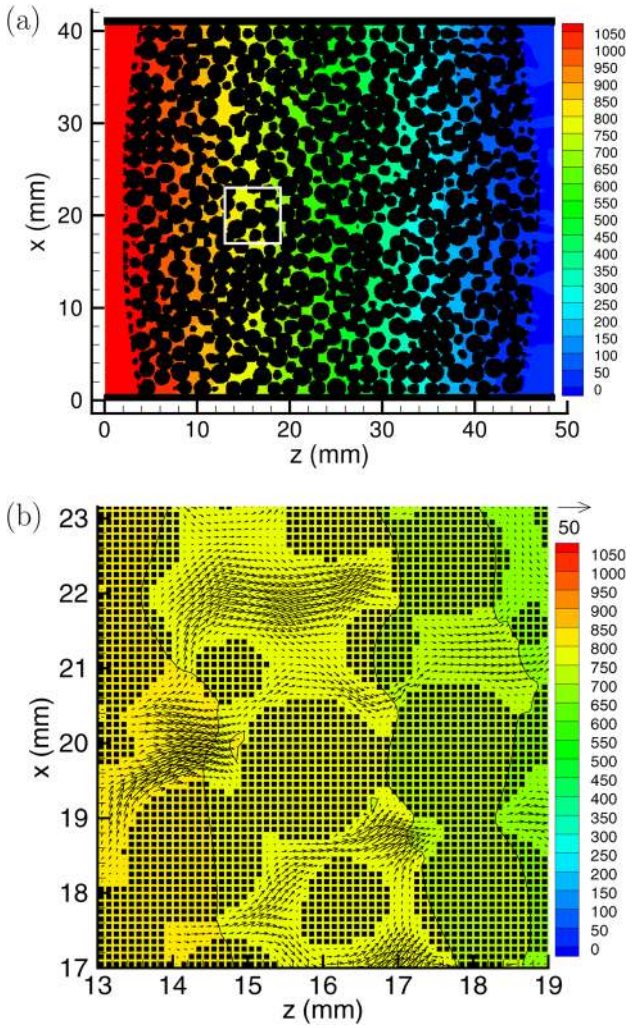


**Fig. 5 (*a*) An *xz* cross section of the flow and pressure field inside the permeability cell, as obtained from a simulation with the stress IBM at 0.1 mm resolution (the same resolution as was used for the X-ray CT scan). The color denotes the pressure in Pa (assuming a fluid mass density of 1170 kg/m$^3$) with a contour interval of 50 Pa. (*b*) Enlargement of the white box in (*a*). The reference vector represents a velocity of 50 mm/s.**

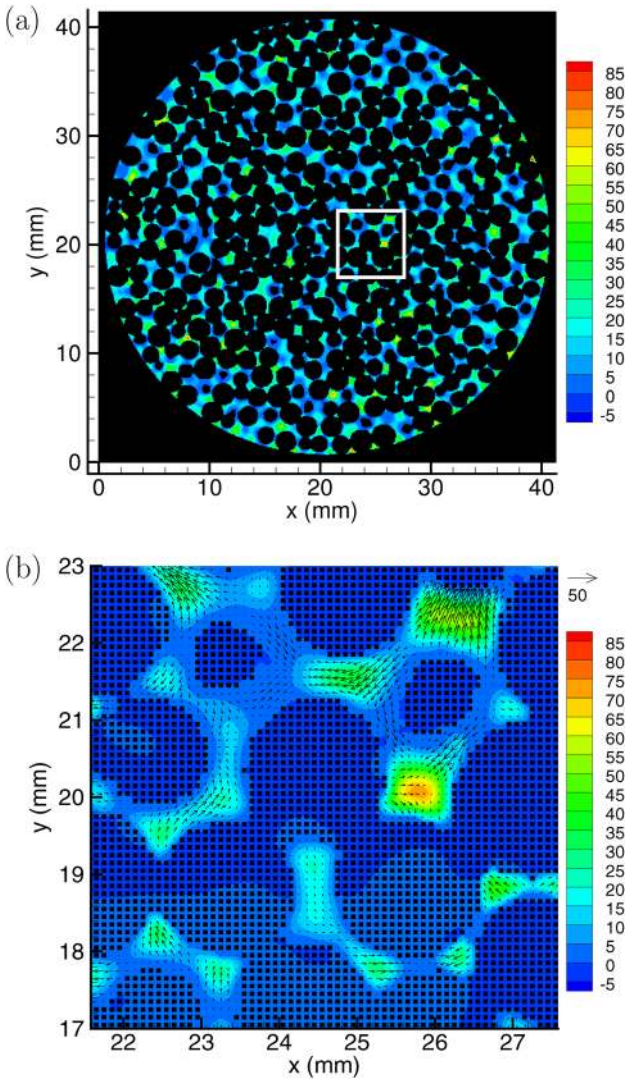


**Fig. 6 The same as in Fig. 5, but for an *xy* cross section of the permeability cell. The color denotes the streamwise velocity in mm/s.**

numerical scheme. Furthermore, while the fluid-solid interfaces are smoothed in the volume penenalization IBM, the interfaces remain sharp in the stress IBM and, hence, higher spatial accuracy may be expected for this IBM.

Finally, we would like to mention that the stress IBM can be applied to both laminar and turbulent flows. Breugem and Boersma [3] applied the stress IBM to study turbulent channel flow over a porous medium composed of a three-dimensional array of cubes. They reported that the maximum penetration velocities through the top layer of cubes (where the flow in between the cubes was turbulent) was on the order of $10^{-5}$ times the channel bulk velocity and thus negligible.

## 5 Numerical Results

Simulations have been performed with both IBMs for the 'standard case' in which the spatial grid resolution is chosen exactly equal to the resolution of the X-ray CT scan, i.e., a grid spacing of 0.1 mm. Figure 5 shows an *xz* cross section of the flow and pressure field as obtained from the stress IBM. Figure 5(*b*) is an enlargement of the white rectangle in Fig. 5(*a*). Similarly, Fig. 6 shows an *xy* cross section of the flow and pressure field.

From the figures, it can be observed that the fluid has a preference to flow through large pores, as expected. The streamwise velocity appears to vary over a large range; from zero at the fluid-solid interfaces to values as high as 85 mm/s. These extreme values are more than seven times as high than the averaged bulk velocity through the pores, which is equal to $\langle u \rangle^s / \varepsilon = 11.5$ mm/s. Inside the large pores the flow seems to be well resolved, while this may be questionable for small pores with a size of $O(\Delta x)$. For determining the permeability this may, however, not be very serious since the fluid prefers to flow through large pores and they are better resolved. Note from Fig. 5 that the contours of the pressure inside the pores are meandering, i.e., they are not straight. This is the result of the spatial heterogeneity of the packing at the pore-scale and it is consistent with a preference of the fluid to flow through the larger pores.

In order to assess the accuracy of the numerical results, for each IBM three simulations have been performed based on the same CT scan. In every next simulation the resolution was doubled compared to the previous one, so that the grid resolution varied from $d_p/\Delta x = 19.3$ ('standard case') to 77.2. (Note that for $d_p/\Delta x = 77.2$, the number of grid cells was approximately equal to $5.3 \times 10^9$.) Since we had only one CT scan at a resolution of $d_p/\Delta x = 19.3$, a doubling in the resolution was achieved by subdividing every grid cell in eight daughter cells, with all having

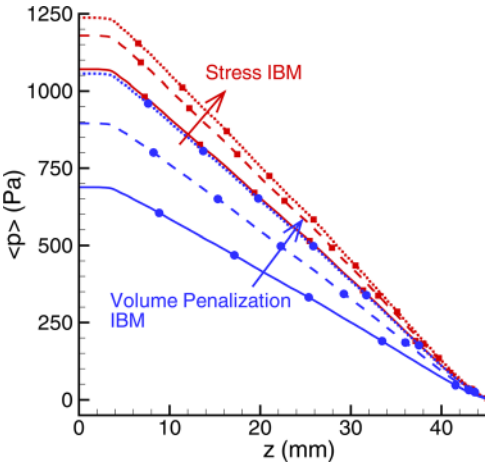


**Fig. 7 The area-averaged intrinsic pressure $\langle p \rangle$ as a function of the streamwise distance $z$. Blue lines/dots: volume penalization IBM. Red line/squares: stress IBM. The lines represent different grid resolutions: —, $d_p/\Delta x = 19.3$; - - -, $d_p/\Delta x = 38.6$; ..., $d_p/\Delta x = 77.2$. The arrows point in the direction of increasing grid resolution.**

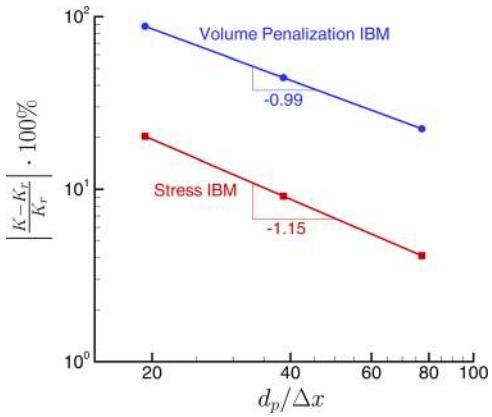


**Fig. 8 Percentage of error in the permeability ($K$) as a function of the grid resolution ($d_p/\Delta x$). The error is relative to the estimated value of the permeability at infinite grid resolution ($K_r$), as obtained from the Richardson extrapolation based on the three data points. Blue line/dots: volume penalization IBM. Red line/squares: stress IBM.**

the same solid volume fraction as the mother cell (either 0 or 1). In fact, this implies that we effectively increased the resolution at which the flow inside the pores is resolved, while the resolution with which the geometry is captured remained fixed at $d_p/\Delta x = 19.3$.

From the simulations, the area-averaged intrinsic pressure $\langle p \rangle$ was computed as function of the streamwise distance $z$. The area-averaged intrinsic pressure was calculated by averaging the pressure at every streamwise position over the pore area of the entire $xy$ cross section of the permeability cell. The area-averaged intrinsic pressure distribution is plotted in Fig. 7 for both IBMs at the three different grid resolutions. Based on Darcy's law and the assumption of macroscopic uniformity of the packing, the intrinsic pressure is expected to drop linearly with the streamwise distance. Indeed, this appears to be the case, substantiating that the packing can be considered as spatially homogeneous in $z$ on a macroscopic scale. Note that the intrinsic pressure is approximately constant at the entrance and exit of the computational domain corresponding to regions outside the glass bead packing. In these regions the flow experiences only a little friction from the wall of the permeability cell, but this is negligible compared to the friction experienced inside the packing of glass beads.

The permeability of the packing has been estimated from the simulations with the help of Eq. (3). The pressure difference over the packing is computed from the drop in the area-averaged intrinsic pressure over the length of the computational domain. For consistency with the analysis of the experimental data, the average streamwise length of the sample is taken to be 42 mm, though Fig. 7 suggests an effective length closer to 41 mm, based on extrapolation of the linear pressure profile in the core of the packing towards the front and the back of the packing. For both IBMs, we obtained the permeability at three different grid resolutions. Next, assuming that the numerical error in the permeability is a power law in the grid resolution, the Richardson extrapolation [27] was applied in order to obtain an estimate of the permeability ($K_r$) at infinite resolution. As can be deduced from the straight lines in Fig. 8, the results indeed confirm this power-law dependency. The estimate of the permeability at infinite resolution for both the volume penalization IBM and the stress IBM is almost exactly the same at $K_r = 2.05 \times 10^{-9}$ m$^2$ and $K_r = 2.06 \times 10^{-9}$ m$^2$, respectively. This is just about 10% less than the experimentally found value of $K_r = 2.27 \times 10^{-9}$ m$^2$.

At finite resolution the stress IBM appears to be much more accurate than the volume penalization IBM: at $d_p/\Delta x = 19.3$ the error in $K$ (as compared to $K_r$) is as large as 88% for the volume penalization IBM, while it is 20% for the stress IBM. The order-of-convergence is also higher for the stress IBM (1.15) than for the volume penalization IBM (0.99). The nearly first-order convergence for the volume penalization IBM can be explained from the smooth interface representation, for which the thickness scales with $\Delta x$. The order of the stress IBM may be surprising since, in the Stokes limit, the stress IBM should produce the same results as a body-fitted method and second-order convergence would be expected. This behavior is presumably related to the sharp straight corners in the staircase representation of the solid-fluid interfaces near which the solution of the Stokes equations becomes singular [28]. If this is correct, then the order-of-convergence will most likely change if the forcing would not be applied to the corner points themselves anymore; the straight corners are then effectively replaced by oblique corners. We have, however, not yet explored this condition.

The fact that $K_r$ is about 10% smaller than the experimentally found value suggests that this difference is related to the apparent resolution with which the solid phase geometry is resolved. If this is true, then the agreement with the experiment can be improved by increasing the resolution of the X-ray CT scan. Interestingly, at $d_p/\Delta x = 38.6$ the numerical error of the stress IBM is about 9% compared to $K_r$, which is close to the 10% error in $K_r$ compared to the experiment. This suggests that an X-ray CT scan resolution of $d_p/\Delta x$ or (50 $\mu$m) and an identical resolution in the numerical simulations, would be close to optimal for improving the accuracy.

## 6 Conclusions

The two direct-forcing IBMs used in this study for computing slow flow through a real porous medium are computationally efficient and capable of reproducing the experimentally determined value of the permeability within an error of 10%. Both IBMs appear to be sensitive to the resolution of the fluid phase in the pores. At finite resolution the stress IBM appears to be much more accurate, as expected. A convergence study suggested that agreement with the experiment could be significantly improved by increasing the resolution of the X-ray CT scan from $d_p/\Delta x = 19.3$ to 38.6.

The numerical simulations yield detailed data on the pore-scale flow field. In a future paper we will present a detailed analysis of the wall-channeling effect near the interface of the packing with the tube wall [20].

## Acknowledgment

The authors would like to thank Wim Verwaal for operating the CT scanner and Cor Gerritsen and Simon Toet for their help with constructing the experimental setup.

## Nomenclature

$C_{ME}$ = constant in modified Ergun equation
$d_p$ = mean particle diameter
$\mathbf{f}$ = additional force from the IBM
$K$ = permeability
$L_c$ = length of glass beads packing
$m$ = weighting function
$\dot{m}$ = mass flow rate
$N_p$ = number of glass beads
$p$ = modified pressure
$\tilde{p}$ = correction pressure
$\langle p \rangle$ = intrinsic volume-averaged pressure
$r$ = radial distance
**rhs** = right-hand side of momentum equation
$R_c$ = radius of cylinder
$\mathrm{Re}_p$ = packed bed Reynolds number
$T$ = temperature
$\mathbf{u}$ = velocity
$\mathbf{u}_{\mathrm{fs}}$ = velocity at fluid-solid interface
$\mathbf{u}^{*}$ = first prediction velocity
$\mathbf{u}^{**}$ = second prediction velocity
$V$ = averaging volume
$\alpha$ = cell solid volume fraction
$\gamma$ = phase-indicator function
$\Delta t$ = computational time step
$\Delta x, \Delta y, \Delta z$ = grid cell dimensions
$\varepsilon$ = porosity
$\mu$ = dynamic viscosity
$\nu$ = kinematic viscosity
$\rho$ = fluid mass density

## References

[1] Sahraoui, M. and Kaviany, M., 1992, "Slip and No-Slip Velocity Boundary Conditions at Interface of Porous, Plain Media," Int. J. Heat Mass Transfer, **35**(4), pp. 927–943.
[2] Zick, A. A. and Homsy, G. M., 1982, "Stokes Flow Through Periodic Arrays of Spheres," J. Fluid Mech., **115**, pp. 13–26.
[3] Breugem, W.-P., and Boersma, B., 2005, "Direct Numerical Simulations of Turbulent Flow Over a Permeable Wall Using a Direct and a Continuum Approach," Phys. Fluids, **17**(2), p. 025103.
[4] Narsilio, G. A., Buzzi, O., Fityus, S., Yun, T. S., and Smith, D. W., 2009, "Upscaling of Navier–Stokes Equations in Porous Media: Theoretical, Numerical and Experimental Approach," Comput. Geotech., **36**, pp. 1200–1206.
[5] Kaczmarczyk, J., Dohnalik, M., Zalewska, J., and Cnudde, V., 2010, "The Interpretation of X-ray Computed Microtomography Images of Rocks as an Application of Volume Image Processing and Analysis," Proceedings of the WSCG 2010—Communication Papers, pp. 23–30.
[6] Kaczmarczyk, J., Dohnalik, M., and Zalewska, J., 2010, "Three-Dimensional Pore Scale Fluid Flow Simulation Based on Computed Microtomography Carbonate Rocks' Images," Fifth European Conference on Computational Fluid Dynamics (ECCOMAS CFD 2010).
[7] Zaretskiy, Y., Geiger, S., Sorbie, K., and Förster, M., 2010, "Efficient Flow and Transport Simulations in Reconstructed 3D Pore Geometries," Adv. Water Res., **33**, pp. 1508–1516.
[8] Ovaysi, S. and Piri, M., 2010, "Direct Pore-Level Modeling of Incompressible Fluid Flow in Porous Media," J. Comput. Phys., **229**, pp. 7456–7476.
[9] Gerbaux, O., Buyens, F., Mourzenko, V. V., Memponteil, A., Vabre, A., Thovert, J.-F., and Adler, P., 2010, "Transport Properties of Real Metallic Foams," J. Colloid Interface Sci., **342**, pp. 155–165.
[10] Mittal, R. and Iaccarino, G., 2005, "Immersed Boundary Methods," Annu. Rev. Fluid Mech., **37**, pp. 239–261.
[11] Smolarkiewicz, P. K. and Winter, C. L., 2010, "Pores Resolving Simulation of Darcy Flows," J. Comput. Phys., **229**, pp. 3121–3133.
[12] Lopez Penha, D. J., Geurts, B. J., Stolz, S., and Nordlund, M., 2011, "Computing the Apparent Permeability of an Array of Staggered Square Rods Using Volume-Penalization," Comput. Fluids, **51**, pp. 157–173.
[13] Kajishima, T., Takiguchi, S., Hamasaki, H., and Miyake, Y., 2001, "Turbulence Structure of Particle-Laden Flow in a Vertical Plane Channel Due to Vortex Shedding," JSME Int. J., Ser. B, **44**(4), pp. 526–535.
[14] Pourquie, M., Breugem, W.-P., and Boersma, B. J., 2009, "Some Issues Related to the Use of Immersed Boundary Methods to Represent Square Obstacles," Int. J. Multiscale Comp. Eng., **7**(6), pp. 509–522.
[15] Bear, J., 1988, *Dynamics of Fluids in Porous Media*, Dover, New York.
[16] Whitaker, S., 1999, *The Method of Volume Averaging*, Kluwer, Dordrecht, The Netherlands.
[17] Bird, R. B., Stewart, W. E., and Lightfoot, E. N., 2002, *Transport Phenomena*, John Wiley and Sons, New York.
[18] MacDonald, I. F., El-Sayed, M. S., Mow, K., and Dullien, F. A. L., 1979, "Flow Through Porous Media: The Ergun Equation Revisited," Ind. Eng. Chem. Fundam., **18**(3), pp. 199–208.
[19] Gupte, A. R., 1970, "Experimentelle Untersuchung der Einflüsse von Porosität und Korngrößenverteilung im Widerstandsgesetz der Porenströmung," Ph.D. thesis, Karlsruhe Institute of Technology, Karlsruhe, Germany.
[20] Vafai, K., 1984, "Convective Flow and Heat Transfer in Variable-Porosity Porous Media," J. Fluid Mech., **147**, pp. 233–259.
[21] Song, C., Wang, P., and Makse, H., 2008, "A Phase Diagram for Jammed Matter," Nature (London), **453**, p. 629632.
[22] Cheng, N. S., 2008, "Formula for the Viscosity of a Glycerol-Water Mixture," Ind. Eng. Chem. Res., **47**(9), pp. 3285–3288.
[23] Harlow, F. H. and Welch, J. E., 1965, "Numerical Calculation of Time-Dependent Viscous Incompressible Flow of Fluid With Free Surface," Phys. Fluids, **8**(12), pp. 2182–2189.
[24] Wesseling, P., 2001, *Principles of Computational Fluid Dynamics* (Springer Series in Computational Mathematics), Vol. 29, Springer-Verlag, Berlin.
[25] Scotti, A., 2006, "Direct Numerical Simulation of Turbulent Channel Flows With Boundary Roughened With Virtual Sandpaper," Phys. Fluids, **18**, p. 031701.
[26] Belliard, M. and Fournier, C., 2010, "Penalized Direct Forcing and Projection Schemes for Navier–Stokes," C.R. Acad. Sci., Ser. I, **348**, pp. 1133–1136.
[27] Ferziger, J. H. and Perić, M., 2002, *Computational Methods for Fluid Dynamics*, Springer-Verlag, Berlin.
[28] Mustakis, I. and Kim, S., 1998, "Microhydrodynamics of Sharp Corners and Edges: Traction Singularities," AIChE J., **44**, pp. 1469–1483.